Available online at www.sciencedirect.com
SCIENCE DIRECT
Physica C 437–438 (2006) 69–72
PHYSICA C
www.elsevier.com/locate/physc

Anisotropic avalanches and flux penetration in patterned superconductors

Diana G. Gheorghe [a,*], Mariela Menghini [a], Rinke J. Wijngaarden [a], Sophie Raedts [b], Alejandro V. Silhanek [b], Victor V. Moshchalkov [b]

[a] Department of Physics and Astronomy, Vrije Universiteit, De Boelelaan 1081, 1081 HV Amsterdam, The Netherlands
[b] Nanoscale Superconductivity and Magnetism Group, Laboratory for Solid State Physics and Magnetism, K. U. Leuven, Celestijnenlaan 200D, B-3001, Leuven, Belgium

Available online 25 January 2006

Abstract

Both for a fundamental understanding of the flux penetration process and for technical applications, the role of artificial pinning sites (such as antidots) in superconductors generates a lot of interest. We perform magneto-optical imaging experiments on type-II Pb thin films patterned with square arrays of square antidots and square arrays of rectangular antidots and blind holes. We demonstrate that a square lattice of rectangular antidots can lead to similar anisotropy in flux penetration and critical current as a rectangular lattice of square antidots. In addition we show how thermo-magnetic avalanches can be guided—and hence to a certain extend controlled—by such holes.

PACS: 74.25.Qt

Keywords: Vortex dynamics; Periodic pinning; Vortex avalanches

1. Introduction

Superconductors patterned with periodic arrays of columnar defects [1], antidots (holes that fully penetrate the sample) [2–5,7–9] and blind holes (holes that partially penetrate the sample) [10] have been extensively studied. These systems are optimal to study fundamental problems related to vortex pinning such as defect-vortex interactions and the influence of the strength and density of the pinning centers on the morphology and dynamics of the vortex lattice. Moreover, they open perspectives for practical applications such as enhancement of the critical current [11], noise reduction in SQUIDS [12] and ratchet effects [13,14]. Experimental studies on superconducting films patterned with square [5,9], triangular [3] and rectangular [7] arrays of antidots, reveal that the vortices move inside the sample preferentially along the principal directions of the antidot lattice, leading to anisotropic flux patterns and anisotropic critical currents [4–6]. Calculations have reproduced qualitatively the experimentally observed anisotropy [15,16]. In most previous studies the anisotropy in the flux penetration is due to the anisotropic properties of the antidot array. In this paper we show that similar anisotropy in flux penetration and critical current can be induced by the anisotropy of the pinning sites themselves: a square array of rectangular holes can lead to a similar anisotropy as a rectangular array of square holes. We perform numerical simulations that support the experimental observations. Additionally, we show that the avalanches resulting from thermomagnetic instabilities [17–20] can be guided by the antidot array.

2. Experimental technique and sample preparation

Magneto-optical imaging experiments have been carried out on Pb thin films, $T_c = 7.2$ K, patterned with square arrays of square antidots (sample S1, width $w = 1.6$ mm,

* Corresponding author.
E-mail address: d.gheorghe@few.vu.nl (D.G. Gheorghe).

0921-4534/$ - see front matter © 2006 Elsevier B.V. All rights reserved.
doi:10.1016/j.physc.2005.12.021

length $L = 2.9$ mm, thickness $h = 65$ nm), square arrays of rectangular antidots (sample S2, $w = 1.8$ mm, $L = 2.4$ mm, $h = 50$ nm) and square arrays of rectangular blind holes (sample S3, $w = 2.3$ mm, $L = 2.7$ mm, $h = 50$ nm). The period of the square lattice is the same for all three samples: $d = 1.5$ μm. The size of the square antidots is 0.8 μm, while the rectangular antidots and blind holes have the same dimensions, 0.46×0.97 μm^2. The films were prepared by electron-beam evaporation on a Si/SiO_2 substrate in which the nanostructuring had been previously defined by electron beam lithography [10]. The samples patterned with rectangular antidots and blind holes were evaporated simultaneously, thus allowing direct comparison of their pinning properties. Using an advanced magneto-optical technique [21], the flux distribution at the surface of the sample was visualized with a Bi-substituted garnet indicator with a saturation field of 50 mT. The indicator was placed on top of the sample and the assembly was mounted on a custom-designed cryogenic microscope, which was placed in an Oxford Instruments 7 T magnet system.

3. Experimental results and discussion

For all samples, the experiments were performed starting from a zero-field-cooled state, followed by an increase of the external magnetic field, H, in steps of 0.1 mT with a constant sweep rate. The field is applied perpendicular to the thin film sample. As H increases, bundles of vortices nucleating at the edge of the sample advance in avalanches mainly along the directions of the antidot/blind hole rows, driven by the Lorentz force induced by the currents flowing in the sample [3]. The morphology of the flux fronts at $T = 3$ K and $\mu_0 H = 1.1$ mT for samples S2 (rectangular antidots) and S3 (rectangular blind holes) is shown in Fig. 1(a) and (c). The array in the sample is such that the long dimension of the holes is parallel to the horizontal direction in the figure. The overall distribution of the magnetic flux for the two samples is similar at this temperature. At higher temperatures ($T = 5$ K), the morphology of the flux fronts changes significantly, see Fig. 1(b) and (d). In sample S2, patterned with antidots, the vortex motion is guided along one-dimensional stripes, following the underlying antidot lattice, while in S3 (blind holes), the stripes show more side branching. The asymmetric flux penetration in Fig. 1(d) is due to a narrow unpatterned region on one side of the sample. The less defined trajectories and the increased vortex penetration in sample S3 suggest that at higher temperature the blind holes are less effective pinning centers than the antidots.

Previous experiments carried out on circular samples patterned with square [5] and rectangular [7,10] arrays of circular antidots revealed that the flux penetration is strongly influenced by the anisotropy of the (rectangular) antidot lattice. However, a similar effect can be obtained not only by tuning the anisotropy of the *antidot lattice* [7,10] but also by changing the anisotropy of the *individual antidot geometry* (this work).

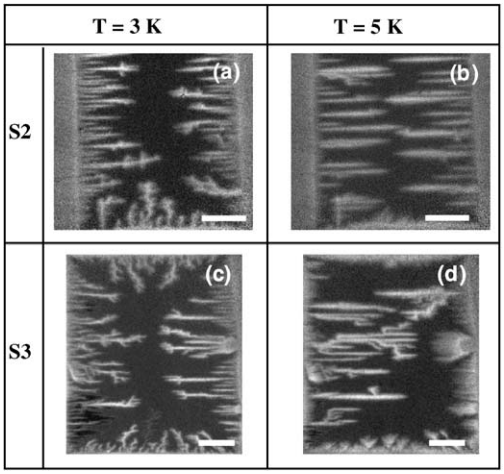

Fig. 1. Flux penetration in samples patterned with rectangular arrays of antidots (sample S2, (a) and (b)) and blind holes (sample S3, (c) and (d)). White areas are regions where magnetic flux is present while black areas correspond to flux free regions. The scale bar corresponds to 0.5 mm.

The resulting anisotropy of critical currents can be calculated [22] from the magneto-optical images of the fully penetrated state, shown in Fig. 2. These images are taken at $T = 6$ K, where avalanches are absent. Since there are no current sources or sinks in the sample, the current flowing parallel to the horizontal and vertical edges are equal. Hence, the ratio between the horizontal and vertical critical current density is $A = j_x/j_y = a/b$, where a and b are the widths over which the currents are flowing (see Fig. 2(d)). For the three samples we obtain $A = 1.1$ (sample S1), $A = 2$ (sample S2) and $A = 1.4$ (sample S3). Clearly, the anisotropy is maximal in the sample patterned with rectangular antidots. This is due to (i) the stronger pinning of the antidots as compared to the blind holes and (ii) the larger anisotropy of the rectangular antidots as compared to the square antidots.

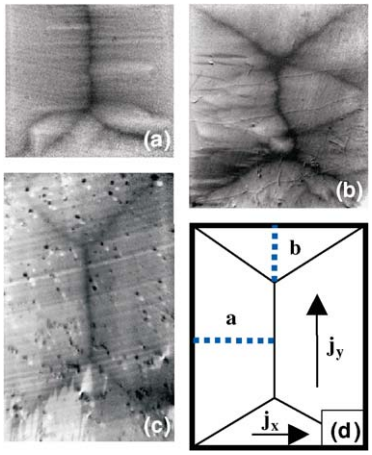

Fig. 2. Samples in the fully penetrated state: (a) S2, (b) S3, (c) S1. All pictures are for the same external conditions, $T = 6$ K and $\mu_0 H = 2.1$ mT. (d) Schematics of the currents flowing in the sample.

4. Numerical simulations

We perform numerical simulations of flux penetration in antidot samples patterned with the same geometries as mentioned above. The simulations are based on the theoretical ideas developed by Brandt [23] and the inversion scheme described in Refs. [24,25]. The Maxwell equations are solved for a conductor with strongly nonlinear conductivity assuming a uniform current distribution along the thickness h of the sample. This assumption implies that the 2D current distribution $\vec{j}(\vec{s})$ can be described by a scalar function g, defined as:

$$\vec{j}(\vec{s}) = \nabla \times \hat{z} g(\vec{s}) \tag{1}$$

where the unit vector $\hat{z}$ is perpendicular to the sample surface. The physical meaning of g is that of the local magnetization of the sample. This current distribution generates a self-field in the sample, whose z-component is given by:

$$\begin{aligned} H_s(\vec{r}) &= \frac{1}{4\pi}\int_A g(\vec{s}) \int_0^h \frac{2(d+\zeta)^2 - |\vec{r}-\vec{s}|^2}{[|\vec{r}-\vec{s}|^2 + (d+\zeta)^2]^{\frac{5}{2}}} d\zeta d^2\vec{s} \\ &=: \int_A Q(\vec{r},\vec{s}) g(\vec{s}) d^2\vec{s} \end{aligned} \tag{2}$$

where A is the area containing the sample surface, $\vec{r}$ is the position in the detector, ζ is the depth in the sample measured from the top surface and d is the distance between the sample and the indicator. $Q(\vec{r},\vec{s})$ is a kernel defined by Eq. (2) [22]. If an external magnetic field $H_a\hat{z}$ is applied, the total z-component of the field experienced by the sample is:

$$H_z(\vec{r}) = H_a + \int_A Q(\vec{r},\vec{s}) g(\vec{s}) d^2\vec{s} \tag{3}$$

Hence, the parameter g can be expressed as

$$g(\vec{s}) = \int_A Q^{-1}(\vec{r},\vec{s})[H_z(\vec{r}) - H_a] d^2\vec{r} \tag{4}$$

Using a Maxwell equation and Eq. (1),

$$\begin{aligned} \dot{B}_z &= \hat{z}\cdot\dot{\vec{B}} = -\hat{z}\cdot(\nabla\times\vec{E}) \\ &= (\hat{z}\times\nabla)\cdot(\rho\hat{z}\times\nabla g) = \nabla\cdot(\rho\nabla g) \end{aligned} \tag{5}$$

where $\vec{B} = \mu_0\vec{H}$ and $\vec{E} = \rho\vec{j}$ and ρ is the nonlinear resistivity of the sample. From the time derivative of Eq. (4) and using (5) we find

$$\dot{g}(\vec{r},t) = \int_A Q^{-1}(\vec{r},\vec{s})\left[\nabla\cdot\left(\frac{\rho}{\mu_0}\nabla g\right) - \dot{H}_a(t)\right] d^2\vec{s} \tag{6}$$

Starting with $g = 0$ everywhere, Eq. (6) is iterated numerically, using the conjugate gradient method to avoid the explicit calculation of Q^{-1} (which has 10^{11} elements!). During the conjugate gradient inversion, g is kept equal to zero outside the sample and constant in the antidots, that is g in a particular antidot is set to the lowest value in the edge of that antidot. This is done to ensure that there is no current outside the sample or in the antidots.

In Fig. 3 the calculated flux profiles are shown for (a) a square array of square antidots and (b) a square array of rectangular antidots. Note that in the simulations the antidots are larger relative to the size of the sample, than in the real samples. This is done in order to have a faster convergence in the numerical calculations. The calculated anisotropy in the current distribution is $A = 1$ for the sample patterned with square antidots and $A = 2$ for the sample with rectangular antidots. From the simulations, we find nearly the same critical current anisotropy as from the magneto-optical experiments. This proves that the observed anisotropy is of a geometrical origin (geometry of the pinning sites) and can be simulated using non-linear electrodynamics.

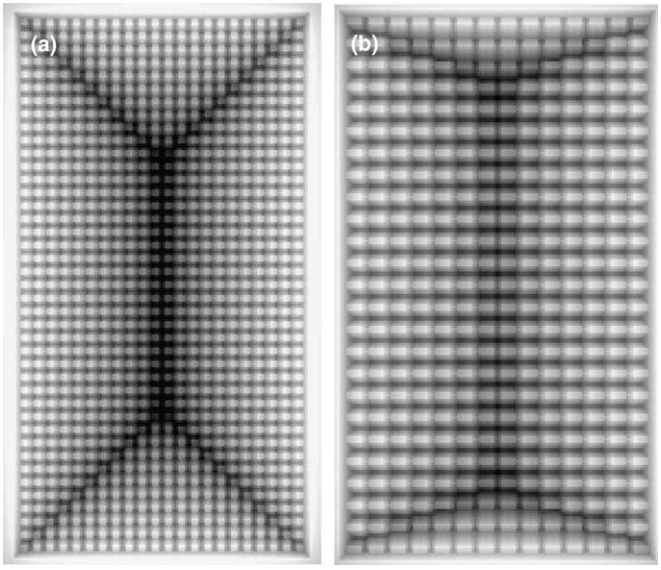

Fig. 3. Simulated flux penetration for a sample patterned with a square lattice of square holes (a) and a square lattice of 1:2 rectangular holes (b).

5. Conclusions

Our magneto-optical experiments on Pb thin films show that antidots provide more efficient guiding of vortices than blind holes. This effect is more pronounced at higher temperatures, where the intrinsic pinning of the sample becomes negligible. Additionally, we have shown that macroscopic anisotropy in the overall flux penetration and current flow can also be induced by a square lattice of anisotropic antidots/blind holes. Results from numerical simulations are consistent with the experimental observations, showing that the antidot induced anisotropy of the critical current is of a purely geometrical origin.

References

[1] (a) J.Y. Lin et al., Phys. Rev. B 54 (1996) 12717;
(b) Th. Schuster et al., Phys. Rev. B 50 (1994) 9499;
(c) V.V. Moshchalkov et al., Phys. Rev. B 57 (1998) 3615.
[2] M. Bezryadin, B. Pannetier, J. Low, Temp. Phys. 98 (1995) 251.
[3] R. Surdeanu et al., Phys. Rev. Lett. 83 (1999) 2054.
[4] L. van Look et al., Physica C 369 (2002) 113.
[5] M. Pannetier et al., Phys. Rev. B 67 (2003) 212501.
[6] M. Menghini et al., Phys. Rev. B 71 (2005) 104506.
[7] M.S. Welling et al., Physica C 404 (2004) 410.

[8] A.V. Silhanek et al., Phys. Rev. B 70 (2004) 054515.
[9] A. Crisan et al., Phys. Rev. B 71 (2005) 144504.
[10] S. Raedts et al., Phys. Rev. B 70 (2004) 024509.
[11] G.W. Crabtree et al., Physica C 387 (2003) 49.
[12] R. Wördenweber, A.M. Castellanos, P. Selders, Physica C 332 (2000) 27.
[13] R. Wördenweber, P. Dymashevski, V.R. Misko, Phys. Rev. B 69 (2004) 184504.
[14] C.C. de Souza Silva et al., Available from: <cond-mat/0506720>, 2005.
[15] C. Reichhardt, G.T. Zimanyi, N. Grønbech-Jensen, Phys. Rev. B 64 (2000) 014501.
[16] C.J. Olson-Reichhardt, C. Reichhardt, Available from: <cond-mat/0401016>, 2004.
[17] I.S. Aranson et al., Phys. Rev. Lett. 94 (2005) 037002.
[18] E. Bonabeau, P. Leiderer, Physica C 256 (1996) 365.
[19] W. Pan, S. Doniach, Phys. Rev. B 49 (1994) 1192.
[20] D.V. Shantsev et al., Phys. Rev. B 72 (2005) 024541.
[21] R.J. Wijngaarden et al., Rev. Sci. Instr. 72 (2001) 2661.
[22] R. Surdeanu et al., Physica C 303 (1998) 191.
[23] E.H. Brandt, Phys. Rev. Lett. 74 (1995) 3025.
[24] R.J. Wijngaarden et al., Phys. Rev. B 54 (1996) 6742.
[25] R.J. Wijngaarden et al., Physica C 295 (1998) 177.